High-pressure behaviour and phase transition of jadarite, a promising B and Li mineral commodity

Davide Comboni[1*], Tommaso Battiston[2], Michael S. Rumsey[3], Francesco Pagliaro[2], Paolo Lotti[2], Michael Hanfland[1], G. Diego Gatta[2]

[1] ESRF − European Synchrotron Radiation Facility, 71 Avenue des Martyrs, CS40220, 38043 Grenoble Cedex, France

[2] Dipartimento di Scienze della Terra, Università degli Studi di Milano, Via Botticelli 23, 20133 Milano, Italy

[3] Department of Mineralogy, Natural History Museum, London SW7 5BD, UK

*** Corresponding Author:** Davide Comboni, current email address davide.comboni@esrf.fr

Davide Comboni: https://orcid.org/0000-0001-6445-3736

Tommaso Battiston: https://orcid.org/0000-0003-1191-1363

Michael S. Rumsey: https://orcid.org/0000-0002-2160-8504

Pagliaro Francesco: https://orcid.org/0000-0001-6483-4205

G. Diego Gatta: https://orcid.org/0000-0001-8348-7181

Paolo Lotti: https://orcid.org/0000-0003-2272-8281

Michael Hanfland: https://orcid.org/0000-0002-8904-5461

Codice campo modificato

Codice campo modificato

Formattato: Inglese (Regno Unito)

Codice campo modificato

Formattato: Inglese (Regno Unito)

Formattato: Inglese (Regno Unito)

Abstract

The high-pressure behaviour of a natural jadarite [ideally $LiNaSiB_3O_7(OH)$, a ~6.76 Å, b ~13.80 Å, c ~7.69 Å, β = 124.09°, Sp. Gr. $P2_1/c$] has been studied by *in-situ* single-crystal and powder synchrotron X-ray diffraction up to 20 GPa, with a diamond-anvil cell and using He as hydrostatic pressure-transmitting fluid. Between 16.57(5) and 17.04(5) GPa, jadarite undergoes a first-order iso-symmetric phase transition, which is reconstructive in character, with a ΔV of about -3%. The structure of the high-pressure polymorph was solved and refined (to R_1 ~ 4%). The isothermal bulk modulus of the low-P polymorph of jadarite is K_{V0} = 55.0(5) GPa (β_{V0}=0.0182(2) GPa^{-1}), and its P-derivative is 3.84(9). The compressional anisotropy, derived along the three main crystallographic directions, is modest, being $\beta_{a0}:\beta_{b0}:\beta_{c0}$ = 1.23:1:1.23. The P-induced deformation mechanisms at the atomic scale, which lead to phase transition, are described.

Keywords: jadarite, borates, lithium commodity, high pressure, phase transition, X-ray diffraction

1. Introduction

Natural borates are the most important source of boron, an important geochemical marker (in particular in pegmatitic and granitic systems) for petrogenetic processes. Jadarite, ideally $LiNaSiB_3O_7(OH)$, is a relatively new mineral species discovered in the Jadar Basin, Serbia. In this sedimentary basin, jadarite occurs in massive white aggregates, several metres thick [1]. Only sporadic subhedral (tabular, elongate) / anhedral crystals (rarely exceeding 5−10 μm) were reported. Jadarite is mainly associated with calcite, dolomite, K-feldspar, rutile, albite, ilmenite, pyrite, and fine-grained muscovite. Minor amounts of searlesite (often intergrown with jadarite), analcime, chlorite, and quartz have also been reported [2]. Its genesis is probably driven by exogenous processes, related to the circulation of hydrothermal fluids [3].

Jadarite, from a marketable point of view, is a unique mineral due to its high content of lithium (*ca.* 7.3 wt% Li_2O) and boron (*ca.* 47.2 wt% B_2O_3). The typical Li_2O grade in exploitable pegmatite deposits (presently the second source of lithium after brines) ranges from about 1.25 to 4.0 wt%, while the massive deposit in the Jadar basin has been estimated at 1Mt with an average Li_2O content of 1.8 wt% [4-6]. Since its discovery, pilot studies and research into processing methods for the extraction of lithium from jadarite have confirmed its economic suitability as a lithium resource [7-8].

Despite the Serbian government has revoked Rio Tinto's exploration licences (January 2022), pushed by recent popular uprisings motivated by environmental and political concerns (Vasovic 2021, Ambrose 2022), the rise of the lithium demand might eventually lead to the exploitation of the jadarite mines which are expected to produce 58,000 tonnes of refined battery-grade lithium carbonate per year. This, accordingly Rio Tinto chairman, Simon Thompson, will allow to satisfy about 90% of the current European needs for lithium. On May 2022, Rio Tinto expressed its will to restart negotiations with the Serbian government (Spasíc 2022).

Increase in demand of lithium worldwide is driven mainly by the battery and power storage industry, the production of which has increased considerably in the last decade [9]. As a result, the global production of lithium commodities has experienced rapid growth: in only 3 years, from 2016 to 2019, estimated world production doubled [9]. Furthermore, as Li- and B-bearing minerals are classified as critical raw materials [10-11]: jadarite will be mainly exploited for its lithium content, but we cannot exclude the exploitation of boron as a relevant by-product.

Although borates are used in more than 300 applications, the production of ceramics, detergents (in particular boric acid), fertilizers, and glass accounts for more than 75% of consumption [9]. Borates are also being used for the production of radiation-shielding materials, as the ^{10}B isotope (~20% of the natural boron) is able to absorb thermal neutrons through the $^{10}B(n,\alpha)^{7}Li$ reaction (~3840 barns), due its high neutron cross section [12-13]. Jadarite (or even its Li-depleted waste), with a high B_2O_3 content, could be added to concretes and epoxy resins to enhance the shielding efficiency against neutron radiation. A series of recent studies have reported this for other natural borates (*e.g.,*[14-23])

To date, the only chemical and crystallographic data of jadarite are those reported in two companion papers by Whitfield *et al*. and Stanley *et al.* [1,2]. Its structural model is based on X-ray powder diffraction data (isotropic model), as single-crystals suitable for X-ray diffraction experiments were not found. In addition, no experiments were performed on jadarite at non-ambient conditions: its principal thermodynamic parameters (*i.e*., volume thermal expansion and compressibility) are still unknown, along with its thermal/compressional anisotropy, d~~i~~ehydroxylation conditions and, more generally, its *P/T* stability field. The aim of this study is to re-investigate of the crystal structure of jadarite based on single-crystal synchrotron X-ray diffraction data and determine its compressional behaviour by powder and single-crystal X-ray diffraction under hydrostatic conditions.

1.2 Crystal structure of jadarite

The crystal structure of jadarite (Fig. 1) was solved by [1] on the basis of X-ray powder diffraction data and described in the space group $P2_1/c$, with a~6.76, b~13.80, c~7.69Å and β~124.09°. It consists of two-dimensional layers, parallel to (010), made of corner-sharing BO_4 and SiO_4 tetrahedra, which form distorted 6-membered rings (6mR) with $(6^4\cdot4^2)(6^2\cdot4)_2$ topology [1] (Fig. 1). The LiO_4 tetrahedron fills the 6mR hole, with a bonding configuration shown in Fig. 1. These layers are mutually connected by distorted Na-octahedra and planar BO_3 units, which share corners with the BO_4 and LiO_4 tetrahedra [1] . The resulting crystalline edifice is shown in Fig. 1. The position of the unique H site in the structure was obtained by *ab initio* optimization [1]: the H atom is bonded to the oxygen atom (O8, Fig. 1) at the apex of the BO_3 group (shared with the LiO_4 tetrahedron), forming a~~n~~ hydroxyl group. Overall, the jadarite structure has no known analogues [1].

Figure 1: From top to bottom: a) schematic view of the two polymorphs of jadarite (left, jadarite; right, jadarite-II); b) Li-migration as consequence of the first order phase transition (Li-site is *orange* in jadarite and *purple* in jadarite-II, respectively; c) Schematic view of the jadarite framework, basically unaffected by the phase transition. Na-atoms in *yellow*, Si-tetrahedra in *blue*, B-O units in *green*, Li-tetrahedra in *red*.

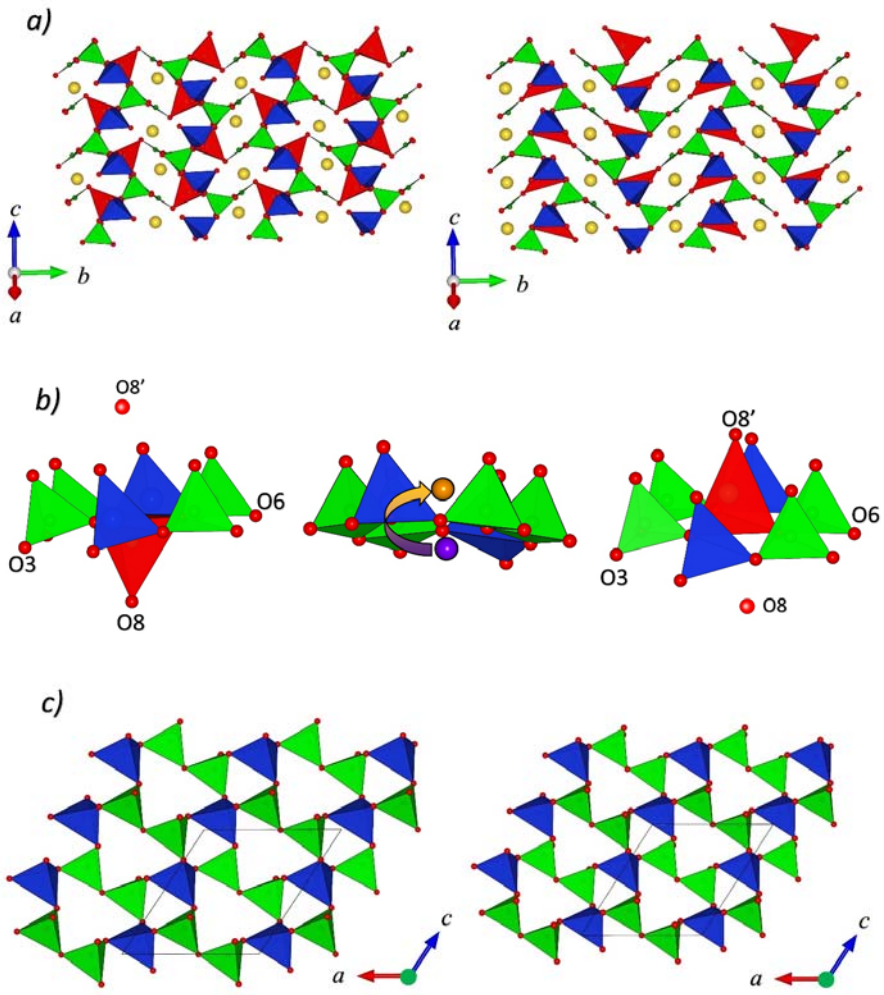

Formattato: Tipo di carattere: Corsivo

Formattato: Tipo di carattere: Corsivo

2. Experimental procedures

The sample of jadarite (a polycrystalline aggregate of about 1g) was kindly provided by the Natural History Museum (London, U.K), the aggregate fragment was from a small batch of fragments (registration number BM2006,22) set aside for research purposes that was from the same parent batch of material used by Whitfield *et al.* and Stanley *et al.* [1-2] for the original study. Two independent high-pressure synchrotron X-ray diffraction experiments were performed: a powder experiment aimed to describe the compressional behaviour of jadarite and a single-crystal experiment aimed to perform structure refinements to describe the deformation mechanisms at the atomic scale. Part of the sample was ground in an agate mortar, whereas a crystal of jadarite (~5x3x2 μm^3) was selected for the single-crystal experiment. The diffraction experiments were performed at the ID15b beamline (ESRF, Grenoble, France) using a convergent monochromatic beam ($E \sim 30$ keV, $\lambda \sim 0.41$ Å, average diameter ~ 9x9 μm). Data were collected with an *Eiger2 9M CdTe* detector, sample-to-detector distance (180 and 250 mm, respectively for the single-crystal and powder experiment) was calibrated using a Si standard and a vanadinite ($Pb_5(VO_4)_3Cl$) crystal. The samples were loaded in membrane-driven diamond anvil cells (DAC), with 600 μm culet Boehler-Almax design anvils, along with a few ruby microspheres as pressure calibrant (pressure uncertainty ± 0.05 GPa, [24]). Helium was used as hydrostatic pressure-transmitting fluid [25]. For the single-crystal experiment, the adopted data collection strategy consisted in a pure ω-scan ($-32° < \omega < +32°$), with 0.5° step width and 0.5 s exposure time per step; for the powder experiment, a single-step ω-scan ($-5° \leq \omega \leq +5°$) with 10 s of exposure time strategy was used.

3. Data analysis

3.1 X-ray Single-crystal diffraction experiment

Indexing of the diffraction peaks and integration of their intensities (corrected for Lorentz-polarization effects) were performed using the *CrysAlisPro* package [26]. Corrections for X-ray absorption effects (by the DAC components) were applied using the semi-empirical *ABSPACK* routine implemented in *CrysAlisPro* [26]. The structure refinements were performed using the package JANA2006 [27], in the space group $P2_1/c$, using the atomic coordinates from Whitfield *et al*. [1] as a starting model. The displacement parameters (D.P.) of all sites were refined as isotropic, as commonly done for high-pressure structure refinements in order to decrease the number of variables; no H-sites were located and refined, due to the poor X-ray scattering power of H. No restraint on bond distances or angles was used. Between

16.57(5) and 17.04(5) GPa (as identified by powder data, described below), jadarite experienced a first-order iso-symmetric phase transition to a high-*P* polymorph stable up to the maximum pressure achieved (~20 GPa). The structure of the high-*P* polymorph was solved using the *Superflip* software [28], implemented in JANA2006 and is herein called jadarite-II. The first structure model was incomplete, but a careful analysis of the difference-Fourier electron density maps allowed the location of the missing atoms. The structure model was refined to a final R_1~0.04. Relevant interatomic distances, average bond lengths, angles, polyhedral volumes, distortion index (defined as $D=\frac{1}{n}\sum_{i=1}^{n}\frac{|l_i-l_{av}|}{l_{av}}$, where l_i is the distance from the central atom to the i^{th} coordinating atom, and $l_{av}$is the average bond length, [29] and bond angle variance [defined as $\sigma^2=\frac{1}{m-1}\sum_{i=1}^{m}(\varphi_i-\varphi_0)^2$, where m is the number of faces in the polyhedron × 3/2 - *i.e.*, number of bonds angles-, φ_i is the i^{th} bond angle and φ_0 is the ideal bond angle for a regular polyhedron] have been calculated using the tools implemented in the VESTA software [30], and are listed in Table 2 and Table S1. The latter, along with CIFs (crystallographic information files) are deposited as Supplementary material.

Figure 2: Evolution of the unit-cell parameters (*a, b, c, β, V*) of jadarite based on X-ray powder diffraction data: unit-cell volume in *black squares*, *a* in *red spheres, b* in *blue diamonds*, *c* in *downwards green triangles, β* in *upwards orange triangles.*

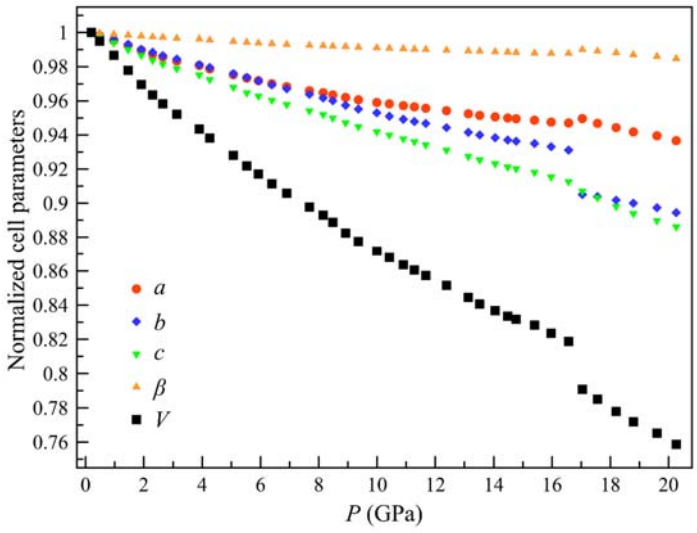

Table 1: Unit-cell parameters of jadarite with pressure, as obtained by X-ray powder diffraction data (*jadarite-II)

P(GPa)	*a* (Å)	*b* (Å)	*c* (Å)	*β* (°)	*V* (Å^3)
0.0001	6.7647(2)	13.808(1)	7.686(1)	124.07(1)	594.7(1)
0.20(5)	6.7566(2)	13.789(1)	7.6812(3)	124.062(2)	592.84(4)
0.48(5)	6.7444(2)	13.768(1)	7.6634(3)	124.017(2)	589.81(4)
0.97(5)	6.7247(2)	13.733(1)	7.6340(3)	123.934(2)	584.95(4)
1.46(5)	6.7049(3)	13.694(1)	7.6038(4)	123.868(3)	579.69(3)
1.91(5)	6.6865(4)	13.653(1)	7.5783(5)	123.809(4)	574.82(4)
2.30(5)	6.6709(3)	13.629(1)	7.5558(4)	123.744(3)	571.22(3)
2.65(5)	6.6595(3)	13.602(1)	7.5389(5)	123.713(3)	568.04(3)
3.13(5)	6.6437(2)	13.575(1)	7.5179(3)	123.644(2)	564.43(2)
3.90(5)	6.6263(4)	13.529(1)	7.4903(5)	123.595(2)	559.31(3)
4.26(5)	6.6125(3)	13.506(1)	7.4693(4)	123.508(3)	556.20(2)
5.07(5)	6.5897(3)	13.457(1)	7.4344(3)	123.418(2)	550.25(3)
5.53(5)	6.5763(3)	13.426(1)	7.4096(5)	123.350(3)	546.49(4)
5.93(5)	6.5658(3)	13.398(1)	7.3951(4)	123.300(3)	543.73(3)
6.39(5)	6.5540(3)	13.366(1)	7.3761(4)	123.256(3)	540.34(3)
6.90(5)	6.5425(3)	13.335(1)	7.3570(4)	123.206(3)	537.03(3)
7.68(5)	6.5262(4)	13.290(1)	7.3284(5)	123.140(3)	532.21(3)
8.15(5)	6.5182(7)	13.260(1)	7.3122(9)	123.107(6)	529.42(7)
8.48(5)	6.5095(8)	13.238(2)	7.2966(9)	123.069(6)	526.91(7)
8.92(5)	6.4998(3)	13.201(1)	7.2749(4)	123.047(3)	523.22(4)
9.36(5)	6.4902(3)	13.170(1)	7.2576(4)	122.999(3)	520.28(4)
9.99(5)	6.4796(4)	13.141(1)	7.2343(5)	122.957(3)	516.84(5)
10.42(5)	6.4742(4)	13.113(1)	7.2202(5)	122.922(3)	514.52(5)
10.90(5)	6.4671(4)	13.088(1)	7.2032(5)	122.884(3)	511.98(6)
11.28(5)	6.4624(4)	13.070(1)	7.1902(5)	122.856(4)	510.17(6)
11.67(5)	6.4569(5)	13.054(1)	7.1760(5)	122.832(4)	508.25(6)
12.38(5)	6.4473(5)	13.020(1)	7.1519(5)	122.777(4)	504.79(7)
13.13(5)	6.4350(6)	12.982(2)	7.1236(7)	122.728(4)	500.64(8)
13.52(5)	6.4285(5)	12.961(1)	7.1083(6)	122.702(4)	498.40(7)
14.05(5)	6.4227(6)	12.939(2)	7.0906(7)	122.666(5)	496.05(8)
14.48(5)	6.4182(5)	12.921(2)	7.0758(7)	122.640(5)	494.11(8)
14.77(5)	6.4152(5)	12.911(2)	7.0681(7)	122.615(5)	493.10(8)
15.40(5)	6.4094(6)	12.892(2)	7.0520(7)	122.575(5)	491.05(8)
15.97(5)	6.4021(5)	12.867(2)	7.0309(7)	122.547(7)	488.20(8)
16.57(5)	6.3987(6)	12.839(2)	7.0100(9)	122.559(7)	485.38(6)
17.04(5)*	6.4161(7)	12.480(1)	6.9669(4)	122.824(6)	468.79(5)
17.56(5)*	6.3972(6)	12.464(1)	6.9377(5)	122.710(4)	465.45(4)
18.20(5)*	6.3803(7)	12.435(1)	6.8988(6)	122.596(5)	461.13(4)
18.79(5)*	6.3630(6)	12.411(1)	6.8665(7)	122.455(4)	457.56(4)
19.60(5)*	6.3480(5)	12.374(1)	6.8350(6)	122.332(4)	453.66(4)
20.26(5)*	6.3286(5)	12.334(1)	6.8068(5)	122.169(3)	449.76(3)

Table 2: Relevant parameters in jadarite and jadarite-II at increasing *P* (D = distortion index, σ^2 =bond angle variance), based on the single-crystal structure refinements (*jadarite-II).

P (GPa)	V_{B1}(Å^3)	σ^2_{B1}	V_{B2}(Å^3)	σ^2	<B3-O> (Å)	D_{B3}	V_{Li}(Å^3)	σ^2_{Li}
0.0001	1.644(2)	2.2	1.660(2)	1.1	1.374(6)	0.01	3.617(4)	80.5
1.04(5)	1.637(2)	2.8	1.647(3)	2.0	1.374(8)	0.01	3.585(5)	83.4
3.19(5)	1.601(3)	3.2	1.645(3)	0.8	1.373(9)	0.01	3.41(1)	101.4
5.30(5)	1.611(2)	2.4	1.627(3)	1.2	1.373(8)	0.01	3.310(5)	90.9
6.80(5)	1.596(3)	3.0	1.623(3)	1.8	1.371(9)	0.01	3.21(1)	94.7
8.41(5)	1.588(3)	3.9	1.615(4)	2.2	1.368(9)	0.01	3.17(1)	117.2
10.17(5)	1.580(2)	4.1	1.618(3)	3.0	1.366(8)	0.01	3.08(1)	94.3
12.03(5)	1.574(3)	4.5	1.609(4)	6.1	1.36(1)	0.02	3.02(1)	104.0
14.57(5)	1.566(2)	2.6	1.571(3)	6.1	1.368(9)	0.01	2.90(1)	94.2
15.81(5)	1.560(2)	2.5	1.575(4)	7.1	1.363(9)	0.01	2.85(1)	92.7
16.60(5)*	1.571(1)	8.5	1.564(2)	6.0	1.379(7)	0.01	3.102(5)	299.8
17.05(5)*	1.555(2)	11.0	1.561(4)	11.4	1.380(9)	0.01	3.080(5)	318.0

	V_{Si}(Å^3)	σ^2_{Si}	V_{Na}(Å^3)	D_{Na}	O4-O7-O3(°)	O7-O3-O1(°)
0.0001	2.175(2)	14.6	31.0(1)	0.1	159.9(2)	74.2(1)
1.04(5)	2.181(3)	17.5	30.3(1)	0.1	160.6(3)	73.9(2)
3.19(5)	2.156(3)	20.6	28.6(1)	0.1	163.1(3)	72.7(2)
5.30(5)	2.144(3)	24.7	27.3(1)	0.1	164.5(3)	72.4(2)
6.80(5)	2.140(3)	26.7	26.3(1)	0.1	165.8(3)	71.7(2)
8.41(5)	2.124(3)	29.4	25.5(1)	0.1	166.6(4)	71.7(2)
10.17(5)	2.109(3)	36.8	24.7(1)	0.1	167.1(3)	71.1(2)
12.03(5)	2.090(4)	41.6	24.1(1)	0.1	167.3(4)	70.8(2)
14.57(5)	2.075(3)	47.2	23.3(1)	0.1	169.4(3)	70.3(2)
15.81(5)	2.073(3)	53.3	22.8(1)	0.1	169.7(3)	69.7(2)
16.60(5)*	2.078(3)	47.4	22.6(1)	0.1	174.1(2)	70.0(2)
17.05(5)*	2.083(4)	49.5	22.4(1)	0.1	174.5(3)	70.0(2)

3.2 X-ray powder experiment

2θ-Intensity patterns have been integrated using the DIOPTAS software [32]. Rietveld full-profile fits have been performed using the GSAS package with the EXPGUI interface [33, 34], using the atomic coordinates reported by Whitfield *et al.* [1] as a starting model for the low-pressure polymorph. The pseudo-Voigt profile function by Thompson *et al.* [35] was used; the background curves were modelled with a Chebyshev polynomial with up to 20 coefficients. Scale factor, unit-cell parameters and the profile peaks coefficients were allowed to vary for all the refinement cycles. Due to the small size of the beam, the intensity of the diffraction peaks was found to be influenced by significant preferential orientation effect, which was corrected. Representative experimental powder patterns are reported in Fig. 3. A first-order *P*-induced phase transition was observed and bracketed between 16.57(5) and 17.04(5) GPa (Fig. 3). A careful inspection of the diffraction patterns of the high-*P* polymorph showed that the phase transition is isosymmetric, with the unit-cell configuration shown in Table 1. The same findings were corroborated by the single-crystal experiment.

Formattato: Tipo di carattere: Corsivo

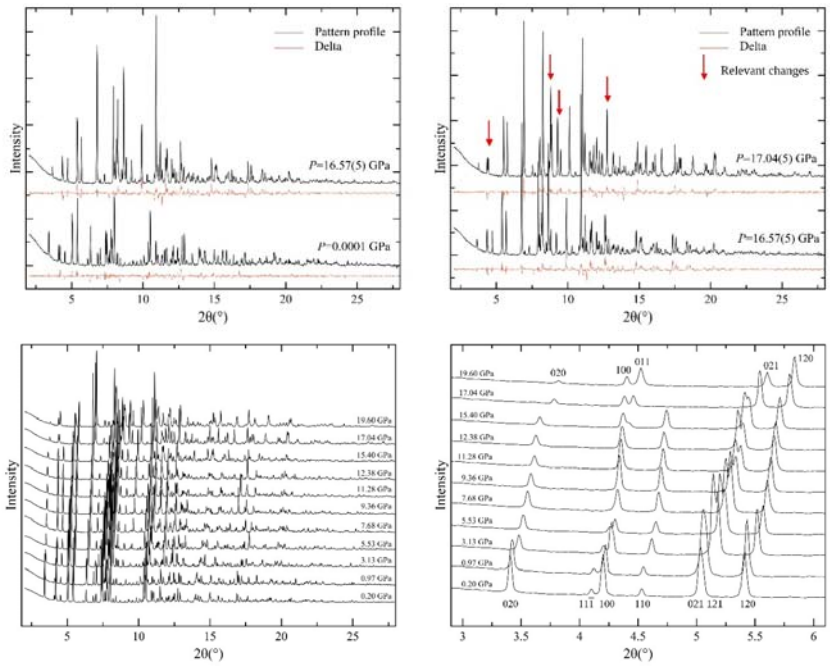

Figure 3: (*Top*) Selected powder X-ray diffraction patterns of jadarite with pressure; Δ, in red line, is calculated as the difference between the observed and the calculated patterns. (*Bottom*) Evolution, with pressure, of the powder pattern of jadarite in which the phase transition was detected between 16.57(5) and 17.04(5) GPa.

3.3 Analysis of the elastic behaviour

The (isothermal) compressional behaviour of the low-pressure polymorph was described using a third-order Birch-Murnaghan Equation of State (BM-EoS; [36]). The BM-EoS allows to refine the bulk modulus (K_{V0} or $K_{P0,T0}$, defined as $-V_0(\partial P/\partial V)_{T0} = \beta^{-1}_{P0,T0}$, where $\beta_{P0,T0}$ is the volume compressibility coefficient at room conditions) and its P-derivatives ($K' = \partial K_{P0,T0}/\partial P$ and $K'' = \partial^2 K_{P0,T0}/\partial P^2$). The BM-EoS parameters were refined minimizing the differences between the EoS curve and the experimental data (weighted by their uncertainties in P and V), using the EOS-FIT7-GUI software [37-38]. Data were fitted considering an estimated uncertainty of ± 0.05 GPa for pressure [24]. For jadarite-II, due to the limited data available, only the average compressibility has been calculated. Elastic parameters are reported in Table 3.

Table 3: Refined elastic parameters pertaining to the different polymorphs of jadarite and to the polyhedra of jadarite-~~II~~, based on the isothermal II- and III-BM Equation of State fits (*fixed parameter).

Jadarite	V_0, x_0 (Å^3, Å)	$K_{V0,}$ (GPa)	K'	$\beta_{V0,\,x0}$ (GPa^{-1})
V	594.7(2)	55.0(5)	3.84(9)	0.0182 (2)
a	6.7546(3)	45(2)	10.7(8)	0.0074(3)
b	13.809(3)	56.0(9)	2.8(1)	0.0060(1)
c	7.686(1)	45.1(4)	2.47(4)	0.00740(6)
				Powder experiment, III-BM EoS, P < 16.57(5) GPa
Jadarite	*Average compressibility per GPa*			Jadarite-II
V	1.1%		*V*	1.3%
a	0.3%		*a*	0.4%
b	0.4%		*b*	0.4%
c	0.5%		*c*	0.7%
				Powder experiment, P > 16.57(5) GPa
Jadarite	V_0 (Å^3)	$K_{V0,}$ (GPa)	K'	$\beta_{V0,\,x0}$ (GPa^{-1})
B1-O_4	1.644(4)	254(11)	4*	0.0039(2)
B2-O_4	1.664(3)	271(20)	4*	0.0037(3)
Li-O_4	3.68(2)	39(1)	4*	0.0256(7)
Si-O_4	2.187(2)	260(8)	4*	0.0039(1)
Na-O_6	31.56(9)	26.3(6)	4*	0.038(1)
				Single-crystal experiment, II-BM EoS, P < 16.57(5) GPa

4. Results and Discussion

4.1 Elastic behaviour

The evolution of the unit-cell parameters of jadarite with pressure, shown in Fig. 2 and listed in Table 1, appears to be monotonic up to about 16.5 GPa. Above this pressure, a first-order iso-symmetric phase transition (jadarite-to-jadarite-II) occurs. Comparing the unit-cell volumes of the low- and high-*P* polymorphs, a difference of about 3.5% is observed (Table 1): this is comparable to what observed in colemanite ($CaB_3O_4(OH)_3 \cdot H_2O$, ΔV~3.4% at 14.5 GPa, [19]) and is rather modest when compared to other hydrated borates (*e.g.*, meyerhofferite $CaB_3O_3(OH)_5 \cdot H_2O$, ΔV~10% at 3 GPa, [21]). The elastic parameters refined with the EOS-FIT7-GUI software [36] revealed that jadarite is a relatively stiff hydrous borate, with a bulk modulus of about 55 GPa (Table 3), higher than ulexite ($NaCaB_5O_6(OH)_6 \cdot 5H_2O$, 37 GPa, [22] and kernite ($Na_2B_4O_6(OH)_3 \cdot 3H_2O$, 29 GPa, [20]), but lower than colemanite ($CaB_3O_4(OH)_3 \cdot H_2O$, 67 GPa, [19]).

Thanks to the single crystal structure refinements, all the polyhedral volumes were calculated with the software VESTA (Table 2) and their evolution with *P* has been modelled with a second-order Birch–Murnaghan equation of state [36]. The B and Si tetrahedra are almost uncompressible, having a bulk modulus higher than 250 GPa (Table 2), and most of the deformation in response to the applied pressure is accommodated by the compression of Na-polyhedra and Li-tetrahedra, which show significantly lower bulk moduli (*i.e.,* 26 and 39 GPa, respectively) and by the tilting of the 6mR tetrahedral units (*e.g.*, as reflected by the variation of the O4-O7-O3 or O7-O3-O1 angles, Table 2).

4.2 *P*-induced structure deformation and comparison between the low- and high-pressure polymorphs.

The 6mRs, made by two SiO_4 tetrahedra and four BO_4 tetrahedra, deform monotonically with pressure until the phase transition takes place (for instance, the O4-O7-O3 angle increases from 159.9(2)° to 169.7(3)°, Table 2) and, overall, below the phase transition pressure, no major changes are observed in the Si-, Na- and B-tetrahedra, whereas the Li-polyhedron shows an increasing level of deformation in response to the applied pressure.

Above 16.5 GPa, jadarite undergoes a first-order phase transition, the structure of the resultant high-*P* polymorph was solved and refined in $P2_1/c$, with an R_1 agreement factor of about 4%. The structural model for the high-*P* polymorph demonstrates that the *P*-induced phase transition is reconstructive in character. As shown in Fig. 1 and 4, the phase transition leads to

a major re-arrangement of the 6mRs and a displacement of the sodium and lithium sites, leading to a new bonding configuration. Specifically, the Li tetrahedron located in the centre the 6mRs, is extremely compressed below the phase transition (V_{P0}~3.617(4) Å^3, $V_{P=15.81(5)GPa}$ =2.85(1) Å^3). Above the phase transition, even though strongly deformed (as shown by the bond angles variance, σ^2_{Li}, Table 2), the Li-tetrahedron compression is significantly reduced ($V_{P=16.60(5)GPa}$ =3.102(5)Å^3) and its configuration is energetically more favourable, as it can be inferred by the Li-O average bond distances (<Li-O> is 1.79(2) Å at 15.81(5) GPa and 1.88(1) Å at 16.60(5) GPa). In order to achieve this more stable configuration, the lithium site has to migrate of about 1.7 Å across the basal plane of the 6mRs, in order to bond to O8' (equal by symmetry to O8, but referred hereafter as O8' in order to facilitate~~ease the~~ discussion) which, below the phase transition, is at about 3.69(2)Å (Table S1, Fig. 1). This affects the planar triangular boron group, and in particular the oxygen site O8 (Fig. 1), but as the distortion index (D_{B3}) remains constant, this does not lead to any major deformation (Tab. 2) of the BO_3 group. Indeed, the triangular BO_3 group acts as a rigid body during the phase transition, rotating to reach the most favourable configuration in response to the new position of the Li site. In this new configuration, Li still retains a fourfold coordination but is connected to O8' (Li-O8'~1.88(2)Å,) whereas Li-O8 is about 3.29(2) Å (Table S1, Fig. 1). The Li- migration does not affect the SiO_4/BO_4 framework, as it can be seen in Fig. 1, 4. The evidence that the phase transition is triggered by the displacement of the Li site is confirmed by the fact that no other polyhedron is significantly affected. For the BO_4 and SiO_4 units, this can be inferred from the bond angle variance values (σ^2) reported in Table 2. Notably, even the Na-polyhedron does not significantly deform in response to the phase transition: only very minor changes are observed. On the other hand, above the phase transition, the +10% volume increase of the Li-tetrahedron is coupled with a triplication of its σ^2 (Table 2), reflecting a major increase of the Li-tetrahedron deformation.

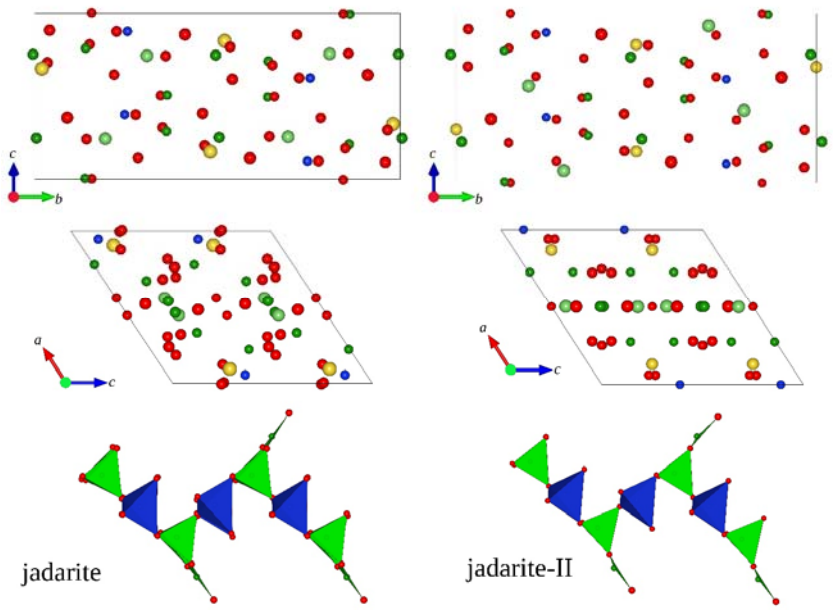

Figure 4: Schematic view along the *a* (top) and *b* (middle) crystallographic axis of (left) jadarite and (right) its high-pressure polymorph, jadarite-II; oxygen sites are in *red*, silicon sites in *blue*, sodium sites in *yellow*, boron sites in *green* and lithium in *light-green*. (bottom) Detail of the endless jadarite-framework resulted from the 6mRs of B- and Si-tetrahedra (respectively in *green* and *blue*).

Contrarily to the other hydrous borates studied so far, the high-pressure phase transition of jadarite does not lead to the increase in coordination of any boron site (*e.g.,* [18,23,39-40]). Furthermore, in the other studies (*e.g.*, meyerhofferite, colemanite, kernite, kurnakovite, ulexite, etc.), the H_2O molecules were key players during the phase transition, as they could be seen as bond-valence moderators (or bond-strength transformer, [41]). Indeed, during the phase transition of the aforementioned borates, at least a fraction of the planar triangular boron groups transforms to tetrahedra by making a new bond with an H_2O molecule [18, 21-23]. However, as jadarite does not contain molecular H_2O, but ~~and~~ only one hydroxyl group per formula unit, its transformation path does not follow those of the aforementioned hydrous borates, this leaving the boron sites with the same coordination scheme in the low- and high-*P* polymorph.

5. Concluding remarks

In this manuscript, the crystal structure of jadarite was re-investigated by single-crystal X-ray diffraction data, and its high-pressure behaviour was studied up to 20 GPa, by means of *in-situ* synchrotron X-ray diffraction experiments. The experimental findings of this study lead to the following concluding remarks:

1) The structural model of jadarite (stable at room conditions), derived on the basis of powder X-ray diffraction data and reported by Whitfield *et al.* [1], is here fully confirmed.
2) Between 16.57(5) and 17.04(5) GPa, jadarite undergoes a first-order iso-symmetric phase transition, with a ΔV of about -3%. The *P*-induced phase transition (which is reconstructive in character) is triggered by the deformation of the 6mR and, in turn, by the compression of the Li-tetrahedron, which reaches an anomalously distorted shape before the phase transition. The Li-tetrahedron appears to be the "weak unit" of the (low-*P*) jadarite structure, which drives the *P*-induced phase transition toward a polymorph in which: *i*) the Li-tetrahedron recovers a bonding configuration that is energetically more favourable and *ii*) the consequent tilting the SiO_4 and BO_4 tetrahedra (composing the 6mRs) leads to a general densification of the structure, better accommodating the effects of the hydrostatic compression.
3) This study provides the first thermodynamic parameters of jadarite. Its isothermal bulk modulus is K_{T0} = 55.0(5) GPa (β_{T0}=0.0182(2) GPa^{-1}), and its *P*-derivative is 3.84(9). The compressional anisotropy of jadarite (derived along the three main crystallographic directions) is modest, being $\beta_{a0}:\beta_{b0}:\beta_{c0}$ = 1.23:1:1.23. Experiments devoted to the thermal behaviour of jadarite will be part of a future study, which would unveil the *T*-stability of this mineral, the de-hydroxylation mechanism and the occurrence of a derived sodium-lithium borosilicate-glass, potentially usable in nuclear-industry vitrification processes for high-level wastes [42].
4) Jadarite is expected to be a future commodity of Li, and potentially B. Given its high Li- and B-content (*ca.* 7.3 wt% Li_2O and 47.2 wt% B_2O_3), jadarite could even be used ("as it is") as a natural Li-B-rich aggregate in Portland cements, because:
    a. Li is known to reduce the deleterious reaction between the alkalis and silica-rich aggregates (the so-called "alkali-silica reactions" – ASR) or minimise damaging expansivity by modifying chemical composition of the reaction products (*e.g.,* [43] and references therein)

b. B is able to provide an efficient neutron-radiation shielding capacity to the concretes (*e.g.*, [14])

This study has shown that the *P*-stability of jadarite far exceeds the typical working conditions of concretes, the determined bulk modulus lies between those of other aggregates usually used in Portland concretes (*e.g.*, calcite ~76 GPa, quartz ~37 GPa) and the low anisotropic behaviour shown by jadarite would be a positive prerequisite for any potential aggregate. In addition, the density of jadarite (*ca*. 2.48 g/cm^3) is relatively low if compared to that of an ordinary Portland cement (usually assumed to be 3.15 g/cm^3), making jadarite a potential "light aggregate".

Acknowledgements

The Natural History Museum (London, U.K) has kindly provided the samples of jadarite, ESRF is thanked for the allocation of the beamtime (https://doi.org/10.15151/ESRF-ES-502121336 and https://doi.org/10.15151/ESRF-ES-502909178). GDG, FP, TB and PL acknowledge the support of the Italian Ministry of Education (MIUR) through the projects "PRIN2017—Mineral reactivity, a key to understand large-scale processes" (2017L83S77). GDG and PL acknowledge the support of the University of Milano through the project "Piano di Sostegno alla Ricerca 2020".

References

[1] Whitfield PS, Le Page Y, Grice JD, Stanley CJ, Jones GC, Rumsey MS, Blake C, Roberts AC, Stirling JAR, Carpenter GJC (2007). Jadarite, $LiNaSiB_3O_7(OH)$, a new mineral species from the Jadar Basin, Serbia. Acta Crystallogr. Sect. B. 63, 396–401.

[2] Stanley CJ, Jones GC, Rumsey MS, Blake C, Roberts AC, Stirling JAR, Carpenter GJC, Whitfield PS, Grice JD, Lepage Y (2007). Jadarite, $LiNaSiB_3O_7(OH)$, a new mineral species from the Jadar Basin, Serbia. Eur. J. Mineral. 19, 575–580.

[3] Stojadinovic U, Matenco L, Andriessen P, Toljić M, Rundić L, Ducea MN (2017). Structure and provenance of Late Cretaceous-Miocene sediments located near the NE Dinarides margin: Inferences from kinematics of orogenic building and subsequent extensional collapse. Tectonophysics, 710, 184-204.

[4] British Geological Survey (2016). Mineral profile Lithium. British Geological Survey, Keyworth, Nottingham (UK)

[5] Bale MD, May AV (1989). Processing of ores to produce tantalum and lithium. Miner. Eng. 2, 299–320.

[6] Vikström H, Davidsson S, Höök M (2013). Lithium availability and future production outlooks. Appl. Energy. 110, 252–266.

[7] Tadesse B, Makuei F, Albijanic B, Dyer L. (2019). The beneficiation of lithium minerals from hard rock ores: A review. Miner. Eng. 131, 170–184.

[8] Rio Tinto (2011). Energy for the Future. Rio Tinto Minerals – Jadar Project factsheet.

Vasovic A. Rio Tinto to pause lithium mine in Serbia after protests. Reuters. December 2021.

Ambrose J. Serbia scraps plans for Rio Tinto lithium mine after protests. The Guardian. January 2022

Vladimir Spasíc. Rio Tinto eager to reopen talks with Serbia on Jadar lithium project. Balkan Green Energy News. May 2022

[9] USGS (2020) Mineral commodity summaries 2020. U.S. Geological Survey, Reston, Virginia (USA)

[10] European Commission, Directorate-General for Internal Market, Industry, Entrepreneurship and SMEs, Study on the review of the list of critical raw materials: final report, Publications Office, 2017, https://data.europa.eu/doi/10.2873/876644

[11] European Commission, Directorate-General for Internal Market, Industry, Entrepreneurship and SMEs, Bobba, S., Carrara, S., Huisman, J., et al., Critical raw materials for strategic technologies and sectors in the EU: a foresight study, Publications Office, 2020, https://data.europa.eu/doi/10.2873/865242

[12] Carter RS, Palevsky H, Myers VW, Hughes DJ (1953). Thermal neutron absorption cross sections of boron and gold. Phys. Rev. 92, 716–721.

[13] Palmer M, Swihart G. (1996). Boron: Mineralogy, Petrology, and Geochemistry, Vol. edited by L. Anovitz & E. Grew, pp. 709–744. Washington: Mineralogical Society of America.

[14] Okuno K (2005) Neutron shielding material based on colemanite and epoxy resin. Radiat. Prot. Dosimetry. 115, 258–261, https://doi.org/10.1093/rpd/ nci154.

[15] Gatta GD, Rotiroti N, Fisch M, Armbruster T (2010). Stability at high pressure, elastic behavior and pressure-induced structural evolution of ''Al_5BO_9'', a mullite-type ceramic material. Phys. Chem. Minerals, 37, 227-236.

[16] Gatta GD, Vignola P, Lee Y (2011). Stability of (Cs,K)$Al_4Be_5B_{11}O_{28}$ (londonite) at high pressure and high temperature: a potential neutron absorber material. Phys. Chem. Minerals 38, 429–434.

[17] Kharita MH, Yousef S, Al Nassar M (2011) Review on the addition of boron compounds to radiation shielding concrete Prog. Nucl. Energy. 53, 2, 207-211. DOI10.1016/j.pnucene.2010.09.012

[18] Lotti P, Gatta GD, Demitri N, Guastella G, Rizzato S, Ortenzi MA, Magrini F, Comboni D, Guastoni A, Fernandez-Diaz MT (2018). Crystal chemistry and temperature behavior of the natural hydrous borate colemanite, a mineral commodity of boron. Phys. Chem. Minerals 45, 405-422.

[19] Lotti P, Gatta GD, Comboni D, Guastella G, Merlini M, Guastoni A, Liermann HP (2017). High-pressure behavior and *P*-induced phase transition of $CaB_3O_4(OH)_3 \cdot H_2O$ (colemanite). J. Am. Ceram. Soc. 100, 2209–2220.

Codice campo modificato

Codice campo modificato

Formattato: Italiano (Italia)

[20] Comboni D, Pagliaro F, Gatta GD, Lotti P, Milani S, Merlini M, Battiston T, Glazyrin K, Liermann HP (2020a) High-pressure behavior and phase stability of $Na_2B_4O_6(OH)_2 \cdot 3H_2O$ (kernite). J Am Ceram Soc 103:5291–5301.

[21] Comboni D, Pagliaro F, Gatta GD, Lotti P, Battiston T, Garbarino G, Hanfland M (2020b). High-pressure behaviour and phase-stability of $Ca_2B_6O_6(OH)_{10} \cdot 2(H_2O)$ (meyerhofferite) Phys. Chem. Minerals 47: 11.

[22] Comboni D, Pagliaro F, Gatta GD, Lotti P, Battiston T, Merlini M, Hanfland M (2021a) Phase transition and high-pressure behavior of ulexite, a potential aggregate in radiation-shielding concretes. Constr Build Mater 291:123188

[23] Pagliaro F, Lotti P, Battiston T, Comboni D, Gatta GD, Camara FA, Milani S, Merlini M, Glazyrin K, Liermann H (2021). Thermal and compressional behavior of the natural borate kurnakovite, $MgB_3O_3(OH)_5 \cdot 5H_2O$. Constr. Build. Mater. 266:121094.

[24] Mao HK, Xu J, Bell PM (1986). Calibration of the ruby pressure gauge to 800 kbar under quasi-hydrostatic conditions J. Geophys. Res. 91, 4673.

[25] Klotz S, Chervin JC, Munsch P, Le Marchand G, (2009) Hydrostatic limits of 11 pressure transmitting media. J Phys D Appl Phys 42(7):075413

[26] Rigaku Oxford Diffraction (2018) CrysAlisPro - Single Crystal X-ray diffraction data collection and processing software (version 1.171.38.46). Rigaku Corporation

[27] Petrícek V, Dušek M, Palatinus L (2014). Crystallographic computing system JANA2006: general features Zeitschrift Fur Krist. 229, 345–352.

[28] Palatinus L, Chapuis G. (2007). SUPERFLIP - a computer program for the solution of crystal structures by charge flipping in arbitrary dimensions. J. Appl. Crystallogr. 40, 786–790.

[29] Baur WH (1974). The geometry of polyhedral distortions. Predictive relationships for the phosphate group. Acta Crystallogr. Sect. B Struct. Crystallogr. Cryst. Chem. 30, 1195–1215.

[30] Momma K, Izumi F (2008). VESTA: a three-dimensional visualization system for electronic and structural analysis. J. Appl. Crystallogr. 41, 653–658.

[31] Prescher C, Prakapenka VB (2015). DIOPTAS: a program for reduction of two-dimensional X-ray diffraction data and data exploration. High Press. Res. 35, 223–230.

[32] Toby BH (2001). "EXPGUI, a Graphical User Interface for GSAS," J. Appl. Crystallogr. 34, 210

[33] Larson AC, Von Dreele RB (2004). Report LAUR 86-748. Los Alamos National Laboratory.

[34] Thompson P, Cox DE, Hastings JB (1987). Rietveld refinement of debye-scherrer synchrotron x-ray data from Al_2O_3. J. Appl. Crystallogr. 20, 79–83.

[35] Birch F (1947). Finite elastic strain of cubic crystals. Phys. Rev. 71, 809–824.

[36] Gonzalez-Platas J, Alvaro M, Nestola F, Angel R (2016). EosFit7-GUI: a new graphical user interface for equation of state calculations, analyses and teaching J. Appl. Crystallogr. 49, 1377–1382.

[37] Angel RJ, Gonzalez-Platas, J, Alvaro, M. (2014). EosFit7c and a Fortran module (library) for equation of state calculations. Zeitschrift Fur Krist. 229, 405–419.

[38] Comboni D, Poreba T, Pagliaro F, Battiston T, Lotti P, Gatta GD, Garbarino G, Hanfland M. (2021b) Crystal structure of the high-P polymorph of $Ca_2B_6O_6(OH)_{10}\cdot 2(H_2O)$ (meyerhofferite). Acta Crystallogr B 77:940–945. https://doi.org/10.1107/S2052520621009768.

[39] Comboni D, Battiston T, Pagliaro F, Lotti P, Gatta GD, Hanfland M (2022) High-pressure behaviour and atomic-scale deformation mechanisms in inyoite, $CaB_3O_3(OH)_5\cdot 4H_2O$. Phys. Chem. Minerals 49: 4.

[41] Hawthorne FC (2012). A bond-topological approach to theoretical mineralogy: crystal structure, chemical composition and chemical reactions. Phys. Chem. Minerals 39, 841–874.

[42] Roderick JM, Holland D, Scales CR (2000). Characterisation and radiation resistance of a mixed alkali borosilicate glass for high level waste vitrification. Phys. Chem. Glass, 41, 392-395.

[43] Zapała-Sławeta J, Owsiak Z (2016) The role of lithium compounds in mitigating alkali-gravel aggregate reaction, Construction and Building Materials, Volume 115, 299-303

Table S1: Inter-tetrahedral angles, cation-anion distances, polyhedral volumes and deformation parameters in jadarite and jadarite-II (D = distortion index, σ^2 =bond angle variance, * data referred to jadarite-II), based on the single-crystal structure refinements.

P (GPa)	O7-O1-O3(°)	O7-O2-O4(°)	O4-O7-O3(°)	O7-O3-O1(°)	O2-O4-O7(°)	O2-O7-O1(°)
0.0001	149.1(2)	151.3(2)	159.9(2)	74.2(1)	71.0(1)	78.7(2)
1.04(5)	149.6(2)	151.6(2)	160.6(3)	73.9(2)	70.9(2)	78.0(2)
3.19(5)	152.1(2)	153.5(2)	163.1(3)	72.7(2)	69.9(2)	76.3(3)
5.30(5)	153.5(2)	154.7(2)	164.5(3)	72.4(2)	69.1(2)	75.3(2)
6.80(5)	154.4(2)	155.9(2)	165.8(3)	71.7(2)	68.6(2)	74.6(2)
8.41(5)	154.8(2)	156.2(3)	166.6(4)	71.7(2)	68.4(2)	74.3(3)
10.17(5)	155.1(2)	156.9(2)	167.1(3)	71.1(2)	67.8(2)	73.6(2)
12.03(5)	155.1(3)	157.2(3)	167.3(4)	70.8(2)	67.7(2)	73.5(3)
14.57(5)	156.0(3)	158.5(3)	169.4(3)	70.3(2)	67.2(2)	72.4(2)
15.81(5)	156.5(4)	158.5(4)	169.7(3)	69.7(2)	67.0(2)	71.9(2)
16.60(5)*	166.2(2)	160.9(3)	174.1(2)	70.0(2)	67.0(1)	68.9(1)
17.05(5)*	166.2(3)	161.1(4)	174.5(3)	70.0(2)	67.0(2)	68.7(2)

P (GPa)	O2-O4-O3(°)	O3-O2-O6(°)	O6-O7-O5(°)	O4-O1-O5(°)	O4-O3-O1(°)	*P* (GPa)
0.0001	76.1(1)	85.9(2)	60.4(1)	85.9(1)	77.5(1)	0.0001
1.04(5)	75.7(2)	85.6(2)	60.6(2)	85.3(2)	77.6(2)	1.04(5)
3.19(5)	74.7(2)	83.7(2)	60.7(2)	83.0(2)	76.7(2)	3.19(5)
5.30(5)	74.3(2)	82.6(2)	60.9(2)	80.7(2)	75.8(2)	5.30(5)
6.80(5)	73.1(2)	81.1(2)	60.8(2)	79.7(2)	75.5(2)	6.80(5)
8.41(5)	72.9(2)	80.6(2)	60.8(2)	79.1(2)	75.6(2)	8.41(5)
10.17(5)	72.2(2)	79.5(2)	60.5(2)	78.2(2)	75.3(2)	10.17(5)
12.03(5)	71.8(2)	78.8(3)	60.3(2)	77.7(2)	75.3(3)	12.03(5)
14.57(5)	71.1(2)	77.8(3)	61.1(2)	77.2(2)	75.3(3)	14.57(5)
15.81(5)	71.0(3)	77.1(3)	61.1(2)	76.4(3)	74.5(3)	15.81(5)
16.60(5)*	73.2 (2)	76.2(2)	60.8(2)	76.0(2)	73.6(2)	16.60(5)*
17.05(5)*	73.0(3)	75.7(3)	60.9(2)	75.4(2)	73.1(3)	17.05(5)*

P (GPa)	B1-O1(Å)	B1-O3(Å)	B1-O5(Å)	B1-O7(Å)	<B-O> (Å)	*V*(Å^3)	σ^2
0.0001	1.473(7)	1.474(8)	1.498(6)	1.452(5)	1.474(7)	1.644(2)	2.2
1.04(5)	1.477(9)	1.47(1)	1.512(8)	1.435(6)	1.473(8)	1.637(2)	2.8
3.19(5)	1.48(1)	1.46(1)	1.495(9)	1.425(8)	1.464(9)	1.601(3)	3.2
5.30(5)	1.464(9)	1.457(9)	1.502(8)	1.436(6)	1.465(8)	1.611(2)	2.4
6.80(5)	1.47(1)	1.45(1)	1.494(9)	1.430(7)	1.460(9)	1.596(3)	3.0
8.41(5)	1.47(1)	1.46(1)	1.49(1)	1.420(8)	1.46(1)	1.588(3)	3.9
10.17(5)	1.47(1)	1.45(1)	1.488(9)	1.418(7)	1.455(9)	1.580(2)	4.1
12.03(5)	1.47(1)	1.45(2)	1.49(1)	1.411(9)	1.45(1)	1.574(3)	4.5
14.57(5)	1.45(1)	1.445(7)	1.48(1)	1.436(5)	1.451(8)	1.566(2)	2.6
15.81(5)	1.45(1)	1.444(7)	1.47(2)	1.432(5)	1.45(1)	1.560(2)	2.5
16.60(5)*	1.483(9)	1.449(5)	1.43(1)	1.455(4)	1.453(9)	1.571(1)	8.5
17.05(5)*	1.49(1)	1.448(7)	1.40(1)	1.453(5)	1.449(8)	1.555(2)	11.0

P (GPa)	B2-O7(Å)	B2-O2(Å)	B2-O4(Å)	B2-O6(Å)	<B-O> (Å)	*V*(Å^3)	σ^2
0.0001	1.450(7)	1.482(7)	1.483(5)	1.501(6)	1.479(6)	1.660(2)	1.1
1.04(5)	1.447(8)	1.472(9)	1.478(7)	1.504(8)	1.476(8)	1.647(3)	2.0
3.19(5)	1.45(1)	1.48(1)	1.471(8)	1.495(9)	1.475(9)	1.645(3)	0.8
5.30(5)	1.447(8)	1.471(9)	1.477(7)	1.482(8)	1.469(8)	1.627(3)	1.2
6.80(5)	1.45(1)	1.47(1)	1.468(8)	1.484(9)	1.468(9)	1.623(3)	1.8
8.41(5)	1.45(1)	1.47(1)	1.459(9)	1.48(1)	1.47(1)	1.615(4)	2.2
10.17(5)	1.45(1)	1.48(1)	1.463(8)	1.481(9)	1.467(9)	1.618(3)	3.0
12.03(5)	1.44(1)	1.49(1)	1.45(1)	1.47(1)	1.46(1)	1.609(4)	6.1
14.57(5)	1.439(7)	1.47(1)	1.471(5)	1.43(1)	1.453(8)	1.571(3)	6.1
15.81(5)	1.440(7)	1.47(1)	1.472(5)	1.43(2)	1.45(1)	1.575(4)	7.1
16.60(5)*	1.450(5)	1.479(9)	1.451(3)	1.42(1)	1.451(6)	1.564(2)	6.0
17.05(5)*	1.449(7)	1.50(1)	1.440(5)	1.42(1)	1.451(8)	1.561(4)	11.4

P (GPa)	B3-O5(Å)	B3-O8(Å)	B3-O6(Å)	<B-O> (Å)	D
0.0001	1.369(6)	1.391(6)	1.361(5)	1.374(6)	0.01
1.04(5)	1.357(7)	1.389(8)	1.375(6)	1.374(8)	0.01
3.19(5)	1.362(9)	1.40(1)	1.362(7)	1.373(9)	0.01
5.30(5)	1.379(8)	1.383(8)	1.358(6)	1.373(8)	0.01
6.80(5)	1.373(9)	1.395(9)	1.346(7)	1.371(9)	0.01
8.41(5)	1.36(1)	1.39(1)	1.350(8)	1.368(9)	0.01
10.17(5)	1.359(8)	1.403(9)	1.337(7)	1.366(8)	0.01
12.03(5)	1.35(1)	1.40(1)	1.328(9)	1.36(1)	0.02
14.57(5)	1.364(8)	1.38(1)	1.362(8)	1.368(9)	0.01
15.81(5)	1.374(9)	1.36(1)	1.359(8)	1.363(9)	0.01
16.60(5)*	1.371(5)	1.39(1)	1.377(6)	1.379(7)	0.01
17.05(5)*	1.377(9)	1.41(1)	1.351(8)	1.380(9)	0.01

P (GPa)	Li-O1	Li-O8	Li-O7	Li-O2	Li-O8’	<Li-O> (Å)	*V*(Å^3)	σ^2
0.0001	1.932(9)	2.05(1)	1.90(1)	1.879(8)	3.85(1)	1.939(9)	3.617(4)	80.5
1.04(5)	1.92(1)	2.04(1)	1.89(2)	1.884(9)	3.83(1)	1.93(1)	3.585(5)	83.4
3.19(5)	1.90(1)	1.99(2)	1.88(2)	1.86(1)	3.81(2)	1.91(2)	3.41(1)	101.4
5.30(5)	1.86(1)	1.98(1)	1.86(2)	1.838(9)	3.77(1)	1.89(1)	3.310(5)	90.9
6.80(5)	1.85(1)	1.95(2)	1.85(2)	1.81(1)	3.76(1)	1.87(2)	3.21(1)	94.7
8.41(5)	1.87(1)	1.90(2)	1.86(3)	1.81(1)	3.78(2)	1.86(2)	3.17(1)	117.2
10.17(5)	1.83(1)	1.91(2)	1.82(2)	1.80(1)	3.71(1)	1.84(2)	3.08(1)	94.3
12.03(5)	1.83(1)	1.87(3)	1.83(3)	1.79(1)	3.72(2)	1.83(2)	3.02(1)	104.0
14.57(5)	1.82(2)	1.83(2)	1.78(1)	1.78(1)	3.69(2)	1.80(2)	2.90(1)	94.2
15.81(5)	1.80(2)	1.84(3)	1.77(1)	1.76(2)	3.69(2)	1.79(2)	2.85(1)	92.7
16.60(5)*	1.864(9)	3.29(1)	1.92(2)	1.854(6)	1.88(2)	1.88(1)	3.102(5)	299.8
17.05(5)*	1.87(1)	3.30(2)	1.92(3)	1.869(8)	1.86(2)	1.88(2)	3.080(5)	318.0

P (GPa)	Na-O4	Na-O6	Na-O5	Na-O3	Na-O6	Na-O5
0.0001	2.325(4)	2.707(4)	2.625(5)	2.254(4)	2.481(5)	2.579(4)
1.04(5)	2.298(5)	2.692(6)	2.622(7)	2.245(5)	2.471(7)	2.557(6)
3.19(5)	2.271(6)	2.678(7)	2.599(9)	2.195(5)	2.426(9)	2.486(7)
5.30(5)	2.244(5)	2.676(6)	2.590(7)	2.170(5)	2.401(7)	2.419(6)
6.80(5)	2.231(5)	2.681(7)	2.584(8)	2.137(5)	2.375(9)	2.382(7)
8.41(5)	2.222(6)	2.691(7)	2.587(8)	2.129(5)	2.354(9)	2.350(7)
10.17(5)	2.203(5)	2.710(6)	2.579(7)	2.107(5)	2.332(8)	2.325(6)
12.03(5)	2.194(6)	2.719(7)	2.582(8)	2.098(6)	2.314(10)	2.302(7)
14.57(5)	2.178(9)	2.714(5)	2.554(4)	2.088(8)	2.317(6)	2.285(5)
15.81(5)	2.170(9)	2.712(5)	2.552(5)	2.069(8)	2.305(6)	2.273(5)
16.60(5)*	2.096(6)	2.663(3)	2.661(4)	2.109(7)	2.271(4)	2.269(4)
17.05(5)*	2.097(8)	2.662(4)	2.666(5)	2.093(8)	2.254(6)	2.255(5)

P (GPa)	Na-O8	Na-O8	<Na-O>	*V*(Å^3)	*D*
0.0001	3.220(5)	3.235(3)	2.678(4)	31.0	0.1
1.04(5)	3.189(6)	3.184(5)	2.657(6)	30.3	0.1
3.19(5)	3.091(8)	3.046(6)	2.599(7)	28.6	0.1
5.30(5)	3.010(6)	2.927(5)	2.555(6)	27.3	0.1
6.80(5)	2.961(7)	2.825(5)	2.522(7)	26.3	0.1
8.41(5)	2.910(7)	2.753(5)	2.500(7)	25.5	0.1
10.17(5)	2.864(7)	2.665(5)	2.473(6)	24.7	0.1
12.03(5)	2.819(8)	2.615(5)	2.455(7)	24.1	0.1
14.57(5)	2.781(7)	2.560(5)	2.435(6)	23.3	0.1
15.81(5)	2.756(7)	2.530(5)	2.421(6)	22.8	0.1
16.60(5)*	2.488(5)	2.488(5)	2.381(4)	22.6	0.1
17.05(5)*	2.483(6)	2.479(6)	2.374(6)	22.4	0.1

P (GPa)	Si-O2	Si-O4	Si-O1	Si-O3	<Si-O> (Å)	*V*(Å^3)	σ^2
0.0001	1.614(4)	1.638(4)	1.616(3)	1.618(4)	1.622(4)	2.175(2)	14.6
1.04(5)	1.617(5)	1.646(5)	1.613(4)	1.620(6)	1.624(5)	2.181(3)	17.5
3.19(5)	1.612(7)	1.632(6)	1.610(5)	1.619(6)	1.618(6)	2.156(3)	20.6
5.30(5)	1.612(5)	1.629(5)	1.610(4)	1.613(5)	1.616(5)	2.144(3)	24.7
6.80(5)	1.611(6)	1.630(5)	1.605(4)	1.615(6)	1.615(5)	2.140(3)	26.7
8.41(5)	1.605(7)	1.631(7)	1.602(5)	1.610(6)	1.612(6)	2.124(3)	29.4
10.17(5)	1.605(6)	1.620(5)	1.602(4)	1.611(6)	1.610(5)	2.109(3)	36.8
12.03(5)	1.600(7)	1.619(7)	1.592(5)	1.611(7)	1.606(7)	2.090(4)	41.6
14.57(5)	1.601(4)	1.616(7)	1.601(3)	1.595(8)	1.603(6)	2.075(3)	47.2
15.81(5)	1.597(5)	1.617(8)	1.603(4)	1.599(8)	1.604(6)	2.073(3)	53.3
16.60(5)*	1.617(3)	1.593(5)	1.62(2)	1.587(6)	1.604(4)	2.078(3)	47.4
17.05(5)*	1.614(5)	1.602(7)	1.610(3)	1.596(7)	1.606(7)	2.083(4)	49.5